Interparticle Interactions and Direct Imaging of Colloidal Phases Assembled from Microsphere−Nanoparticle Mixtures†

Carlos J. Martinez,‡ Jiwen Liu,‡ Summer K. Rhodes,‡ Erik Luijten,‡ Eric R. Weeks,§ and Jennifer A. Lewis*,‡

Department of Materials Science and Engineering, Frederick Seitz Materials Research Laboratory, University of Illinois at Urbana-Champaign, 1304 West Green Street, Urbana, Illinois 61801, and Physics Department, Emory University, Atlanta, Georgia 30322

Received February 10, 2005

We investigate the interparticle interactions, phase behavior, and structure of microsphere−nanoparticle mixtures that possess high size and charge asymmetry.[1] We employ a novel Monte Carlo simulation scheme[2] to calculate the effective microsphere interactions in suspension, yielding new insight into the origin of the experimentally observed behavior.[3] The initial settling velocity, final sediment density, and three-dimensional structure of colloidal phases assembled from these binary mixtures via gravitational settling of silica microspheres in water and index-matched solutions exhibit a strong compositional dependence. Confocal laser scanning microscopy is used to directly image and quantify their structural evolution during assembly. Below a lower critical nanoparticle volume fraction ($\phi_{nano} < \phi^{L,C}$), the intrinsic van der Waals attraction between microspheres leads to the formation of colloidal gels. These gels exhibit enhanced consolidation as ϕ_{nano} approaches $\phi^{L,C}$. When ϕ_{nano} exceeds $\phi^{L,C}$, an effective repulsion arises between microspheres due to the formation of a dynamic nanoparticle halo around the colloids. From this stable fluid phase, the microspheres settle into a crystalline array. Finally, above an upper critical nanoparticle volume fraction ($\phi_{nano} > \phi^{U,C}$), colloidal gels form whose structure becomes more open with increasing nanoparticle concentration due to the emergence of an effective microsphere attraction,[3] whose magnitude exhibits a superlinear dependence on ϕ_{nano}.

Introduction

Colloidal suspensions enjoy widespread use in applications ranging from advanced materials to drug delivery. By tailoring interparticle interactions, one can design colloidal systems for the assembly of ceramics,[4] inks,[5] coatings,[6] photonic band-gap materials,[7−12] and pharmaceutical[13] materials. Despite their broad importance, the structure and phase transitions of the fluid, gel, crystalline, and glassy states have primarily been studied in hard-sphere systems that interact only through infinite repulsion on contact.[14−20] Recently, these studies have been extended by introducing controlled attractions through either the addition of nonadsorbing polymer[21] or temperature change.[22] Confocal laser scanning microscopy (CLSM)[23] is an invaluable tool in these investigations that allows individual particles to be imaged within a three-dimensional assembly in real space.

† Part of the Bob Rowell Festschrift issue.

‡ University of Illinois at Urbana-Champaign.

§ Emory University.

* To whom correspondence should be addressed: jalewis@uiuc.edu.

(1) Tohver, V.; Smay, J. E.; Braem, A.; Braun, P. V.; Lewis, J. A. Nanoparticle halos: A new colloid stabilization mechanism. *Proc. Natl. Acad. Sci. U.S.A.* **2001**, *98*, 8950−8954.

(2) Liu, J.; Luijten, E. Rejection-Free Geometric Cluster Algorithm for Complex Fluids. *Phys. Rev. Lett.* **2004**, *92*, 035504.

(3) Liu, J.; Luijten, E. Stabilization of Colloidal Suspensions by Means of Highly Charged Nanoparticles. *Phys. Rev. Lett.* **2004**, *93*, 247802.

(4) Lewis, J. A. Colloidal Processing of Ceramics. *J. Am. Ceram. Soc.* **2000**, *83*, 2341−2359.

(5) Smay, J. E.; Gratson, G. M.; Shepherd, R. F.; Cesarano, J., III; Lewis, J. A. Directed Colloidal Assembly of 3D Periodic Structures. *Adv. Mater.* **2002**, *14*, 1279−1283.

(6) Martinez, C. J.; Lewis, J. A. Shape Evolution and Stress Development During Latex-Silica Film Formation. *Langmuir* **2002**, *18*, 4689−4698.

(7) Joannopoulos, J. D.; Villeneuve, P. R.; Fans, S. Photonic Crystals: Putting a New Twist on Light. *Nature* **1997**, *386*, 143−149.

(8) Yablonovitch, E. Inhibited Spontaneous Emission in Solid-State Physics and Electronics. *Phys. Rev. Lett.* **1987**, *58*, 2059−2062.

(9) Braun, P. V.; Wiltzius, P. Electrochemically grown photonic crystals. *Nature* **1999**, *402*, 603−604.

(10) Pan, G.; Kesavamoorthy, R.; Asher, S. A. Optically Nonlinear Bragg Diffracting Nanosecond Optical Switches. *Phys. Rev. Lett.* **1997**, *78*, 3860−3863.

(11) Johnson, S. A.; Oliver, P. J.; Mallouk, T. E. Ordered Mesoporous Polymers of Tunable Pore Size from Colloidal Silica Templates. *Science* **1999**, *283*, 963−965.

(12) Burmeister, F.; Schafle, C.; Matthes, T.; Bohmisch, M.; Boneberg, J.; Leiderer, P. Colloid Monolayers as Versatile Lithographic Masks. *Langmuir* **1997**, *13*, 2983−2987.

(13) Muller, R. H. *Colloidal Carriers for Controlled Drug Delivery and Targeting, Modification, Characterization, and In Vivo Distribution*; CRC Press: Boca Raton, FL, 1991.

(14) Biben, T.; Hansen, J. P. Phase Separation of Asymmetric Binary Hard-Sphere Fluids. *Phys. Rev. Lett.* **1991**, *66*, 2215−2218.

(15) Imhof, A.; Dhont, J. K. G. Experimental Phase Diagram of a Binary Colloidal Hard-Sphere Mixture with a Large Size Ratio. *Phys. Rev. Lett.* **1995**, *75*, 1662−1665.

(16) Dinsmore, A. D.; Yodh, A. G.; Pine, D. J. Phase Diagrams of Nearly Hard-Sphere Binary Colloids. *Phy. Rev. Lett.* **1995**, *52*, 4045−4057.

(17) Kaplan, P. D.; Rouke, J. L.; Yodh, A. G.; Pine, A. Entropically Driven Surface Phase Separation in Binary Colloidal Mixtures. *Phys. Rev. Lett.* **1994**, *72*, 582−585.

(18) Barlett, P.; Ottenwill, R. H.; Pusey, P. N. Superlattice Formation in Binary Mixtures of Hard-Sphere Colloids. *Phys. Rev. Lett.* **1992**, *68*, 3801−3804.

(19) Kegel, W. K.; van Blaaderen, A. Direct Observation of Dynamical Heterogeneities in Colloidal Hard-Sphere Suspensions. *Science* **2000**, *287*, 290−293.

(20) van Blaaderen, A.; Wiltzius, P. Real-Space Structure of Colloidal Hard-Sphere Glasses. *Science* **1995**, *270*, 1177−1179.

(21) Hoog, E. H. A. d.; Kegel, W. K.; van Blaaderen, A.; Lekkerkerker, H. N. W. Direct Observation of Crystallization and Aggregation in a Phase-Separating Colloid-Polymer Suspension. *Phys. Rev. E* **2001**, *64*, 021407.

(22) Varadan, P.; Solomon, M. J. Direct Visualization of Long-Range Heterogeneous Structure in Dense Colloidal Gels. *Langmuir* **2003**, *19*, 509−512.

(23) Wilson, T.; Masters, B. R. Confocal Microscopy. *Appl. Opt.* **1994**, *33*, 565−566.

10.1021/la050382s CCC: $30.25
Published on Web 04/19/2005

Several pioneering studies have been carried out to directly probe the structure and dynamics of colloidal crystals,[24,25] glasses,[20,26] and gels[27] using CLSM. van Blaaderen and Wiltzius have investigated the structure of colloidal crystals[24] and glasses assembled from hard-sphere systems.[20] Weitz and co-workers have studied the homogeneous nucleation and growth of colloidal crystals,[25] the dynamics of hard-sphere suspensions near the glass transition,[28,29] aging phenomena in colloidal glasses,[26] and the structure of colloidal gels formed via depletion attraction.[27] Their observations revealed that the gel structure is systematically more open as the depletion attraction between colloids intensifies. Finally, Varadan and Solomon[22] have investigated the structure of dense colloidal gels formed by temperature-induced attractive interactions. They found that while the short-range structure of these gels is similar to that of dense amorphous hard-sphere systems, their long-range structure differs remarkably, with regions exhibiting significant density fluctuations.

In most systems of practical importance, long-range van der Waals forces must be balanced by Coulombic, steric, or other repulsive interactions to provide control over phase behavior, structure, and assembly. Nanoparticle engineering is a new paradigm by which these interactions may be regulated.[1] We recently demonstrated that binary mixtures possessing both size and charge asymmetry, in which microspheres are negligibly charged and nanoparticles are highly charged, experience a rich phase behavior, transitioning from a colloidal gel to a stable fluid and subsequently to a colloidal gel with increasing nanoparticle concentration.[1,30] We further demonstrated that nanoparticle-mediated assembly of dilute binary mixtures on epitaxially patterned substrates could be utilized to create robust three-dimensional (3-D) colloidal crystals.[31] We attributed the stabilizing transition to nanoparticle "haloing" around the microspheres, which serves to mitigate their van der Waals attraction.[1,30] The system stability is ultimately reversed at higher nanoparticle concentrations, where flocculation ensues. Utilizing a novel Monte Carlo algorithm,[2,32] Liu and Luijten were able to study this system by means of computer simulations.[3] They confirmed that the experimental findings could be quantitatively explained from the formation of a nanoparticle halo, resulting from a weak electrostatic colloid−nanoparticle attraction. At higher nanoparticle concentrations, they also recovered an effective colloidal attraction that increases in strength with nanoparticle concentration and ultimately leads to flocculation. Interestingly, the attraction was found to differ from the regular depletion attraction.[33,34] Similar findings were also recently reported by Louis and co-workers.[35]

Here, we investigate the interparticle interactions, phase behavior, and 3-D structure of microsphere−nanoparticle mixtures over a broad composition range by combining this novel Monte Carlo simulation scheme with direct experimental observations. Specifically, both amorphous (gel) and crystalline sediments are created via gravitational settling of microspheres from these mixtures onto flat substrates in aqueous and index-matched solutions. Confocal microscopy is utilized to monitor their assembly in situ as well as to assess their 3-D structure. The use of index-matched solutions, which is required to facilitate 3-D imaging, lessens the van der Waals attraction between silica microspheres in the absence of nanoparticles. Below a lower critical nanoparticle volume fraction ($\phi^{L,C} \sim 10^{-4}$), dense colloidal gels form that exhibit enhanced consolidation with increasing nanoparticle concentration. Between $\phi^{L,C}$ and an upper critical nanoparticle volume fraction ($\phi^{U,C} \sim 2 \times 10^{-3}$), a stable fluid forms from which the microspheres settle into a crystalline array. Finally, above $\phi^{U,C}$, dense colloidal gels are also produced whose structure is more open with increasing nanoparticle additions. Interestingly, the observed phase transitions occur at values of $\phi^{L,C}$ and $\phi^{U,C}$ that are independent of microsphere concentration. These experimental observations are compared to predictions obtained from Monte Carlo simulations, which for this purpose, are extended to treat binary mixtures with larger colloid−nanoparticle size ratio than in ref 3 and index-matched solvent conditions.

Monte Carlo Simulations of Binary Mixtures

Simulation Method. Monte Carlo simulations are carried out to determine the effective microsphere pair potential induced by the nanoparticles in the fluid phase. This effective potential corresponds to a system in which the degrees of freedom of the nanoparticles have been integrated out.[36] Since the induced interaction is additive to the intrinsic van der Waals attraction between the colloids, it can be computed independently. If it is sufficiently repulsive, it can mitigate the attraction and thus stabilize the suspension. The effective interaction is computed from the colloidal pair potential in the dilute colloid limit. Accordingly, large simulation cells are required, resulting in very large numbers of nanoparticles. Indeed, the calculations presented here involved up to 2×10^7 nanoparticles. In addition, the size asymmetry $a_{micro}/a_{nano} = 200$ between the colloidal microspheres and the nanoparticles makes these calculations virtually inaccessible by conventional simulation methods. The geometric cluster Monte Carlo method,[2] which was applied to a similar system (albeit for a size asymmetry that was twice smaller) in ref 3, addresses both issues. The nonlocal character of the particle movements overcomes the jamming problems typically experienced by large species immersed in an environment of smaller particles, whereas the efficiency improvement resulting from the rejection-

(24) van Blaaderen, A.; Wiltzius, P. Growing Large, Well-Oriented Colloidal Crystals. *Adv. Mater.* **1997**, *9*, 833−835.
(25) Gasser, U.; Weeks, E. R.; Schofield, A.; Pusey, P. N.; Weitz, D. A. Real-Space Imaging of Nucleation and Growth in Colloidal Crystallization. *Science* **2001**, *292*, 258−262.
(26) Courtland, R. E.; Weeks, E. R. Direct Visualization of Aging in Colloidal Glasses. *J. Phys.: Condens. Matter* **2003**, *15*, 359−365.
(27) Dinsmore, A. D.; Weitz, D. A. Direct Imaging of Three-Dimensional Structure and Topology of Colloidal Gels. *J. Phys.: Condens. Matter* **2002**, *14*, 7581−7597.
(28) Weeks, E. R.; Crocker, J. C.; Levitt, A. C.; Schofield, A.; Weitz, D. A. Three-Dimensional Direct Imaging of Structural Relaxation Near the Colloidal Glass Transition. *Science* **2000**, *287*, 627−631.
(29) Weeks, E. R.; Weitz, D. A. Properties of Cage Rearrangements Observed near the Colloidal Glass Transition. *Phys. Rev. Lett.* **2002**, *89*, 095704.
(30) Tohver, V.; Chan, A.; Sakurada, O.; Lewis, J. A. Nanoparticle Engineering of Complex Fluid Behavior. *Langmuir* **2001**, *17*, 8414−8421.
(31) Lee, W.; Chan, A.; Bevan, M. A.; Lewis, J. A.; Braun, P. V. Nanoparticle-Mediated Epitaxial Assembly of Colloidal Crystals on Patterned Substrates. *Langmuir* **2004**, *20*, 5262−5270.
(32) Liu, J.; Luijten, E. Generalized Geometric Cluster Algorithm for Fluid Simulation. *Phys. Rev. E*, in press.
(33) Asakura, S.; Oosawa, F. Interaction Between Particles Suspended in Solutions of Macromolecules. *J. Polym. Sci.* **1958**, *33*, 10−24.
(34) Oosawa, F.; Asakura, S. On Interaction Between Two Bodies Immersed in a Solution of Macromolecules. *J. Chem. Phys.* **1954**, *22*, 1255−1256.
(35) Karanikas, S.; Louis, A. A. Dynamic Colloidal Stabilization by Nanoparticle Halos. *Phys. Rev. Lett.* **2004**, *93*, 248303.
(36) Hill, T. L. *Statistical Mechanics: Principles and Selected Applications*; McGraw-Hill: New York, 1956.

free nature of the Monte Carlo steps[2] facilitates the treatment of large numbers of particles.

In the simulations, 10 microspheres are placed in a cell at volume fraction 0.02. The nanoparticle volume fraction is varied from 10^{-4} (4×10^5 particles) to 5×10^{-3} (2×10^7 particles). Accurate statistics are collected for the microsphere pair correlation function $g(r)$ and the effective pair potential is computed via $V_{\text{eff}} = -k_B T \ln g(r)$.

Model. Both the colloids and the nanoparticles are modeled as spherical particles with a hard core and explicit electrostatic interactions. The solvent (water and water/glycerol, respectively) and screening ions are represented as a homogeneous dielectric medium. The electrostatic double-layer interactions are modeled through the Hogg–Healy–Fuerstenau expression.[37,38] For two nanoparticles at a surface separation D, this equation, under constant-potential conditions, reduces to an exponentially decaying repulsive interaction[39]

$$V_{\text{nano-nano}} = \epsilon_0 \epsilon_r \pi \sigma_{\text{nano}} \Psi_{\text{nano}}^2 \ln[1 + \exp(-\kappa D)] \approx \epsilon_0 \epsilon_r \pi \sigma_{\text{nano}} \Psi_{\text{nano}}^2 \exp(-\kappa D) \quad (1)$$

where the approximation is valid for $\kappa D \gg 1$. Ψ_{nano} is the nanoparticle zeta potential (70 mV in aqueous solution, corresponding to a nanoparticle charge $Q = 30e$), κ the inverse screening length (2 nm in aqueous solution), ϵ_0 the vacuum permittivity, and ϵ_r the dielectric constant of the solvent (80 for water and 50 for glycerol/water, respectively). Since the silica spheres are negligibly charged, we ignore the electrostatic interaction between them. However, an electrostatic double-layer interaction arises between the microspheres and nanoparticles, which for large size asymmetry is described by[37]

$$V_{\text{micro-nano}} = \frac{1}{2} \epsilon_0 \epsilon_r \pi \sigma_{\text{nano}} \Psi_{\text{nano}}^2 \ln[1 - \exp(-2\kappa D)] \approx -\frac{1}{2} \epsilon_0 \epsilon_r \pi \sigma_{\text{nano}} \Psi_{\text{nano}}^2 \exp(-2\kappa D) \quad (2)$$

where the approximation is again valid for $\kappa D \gg 1$. Thus, an attraction is induced that is responsible for the formation of a nanoparticle halo. It must be noted that we have employed the "bare" average nanoparticle diameter ($\phi_{\text{nano}} = 6$ nm) in eq 2, whereas in eq 1 we have accounted for the hydration repulsion between nanoparticles by increasing the diameter by 1.5 nm.

Experimental Section

Materials System. Uniform silica microspheres (Geltech, Alachua, FL) serve as the large colloidal species. These microspheres have an average radius a_{micro} of 0.590 ± 0.01 μm, as determined from quantitative image analysis carried out on scanning electron microscopy (SEM) photomicrographs (15 000× magnification), and a density of 2.25 g/cm^3, as determined by helium pycnometry (model AccuPyc 1330, Micrometrics Instrument Corp., Norcross, GA). They exhibit an isoelectric point at pH ~ 2.5 and a zeta potential of approximately 1 mV at pH 1.5, as measured by microelectrophoresis (ZetaSizer 3000, Malvern Instruments, Northborough, MA) on dilute suspensions ($\phi_{\text{micro}} = 1 \times 10^{-5}$). The Debye length ($\kappa^{-1}$) is 1.8 nm under the experimental conditions of interest (pH = 1.5).

Hydrous zirconia nanoparticles (Zr 10/20, Nyacol Products, Ashland, MA) serve as the small colloidal species. These nanoparticles have an average radius a_{nano} of 3 nm (see Figure 1), as determined by X-ray scattering measurements with a reported radius range of 0.5–11 nm.[40,41] Their reported density is 3.65 g/cm^3,[42] and they are supplied in an acidic solution (pH = 0.5) at a volumetric solids loading of 7.4%. At pH = 1.5, they possess a zeta potential of 63 ± 12 mV, as determined by microelectrophoresis (Malvern Zetasizer 3000). This value is in reasonable agreement with the zeta potential of approximately 70 mV estimated from the reported effective charge determined from titration studies[40] using the approach outlined by Gisler et al.[43]

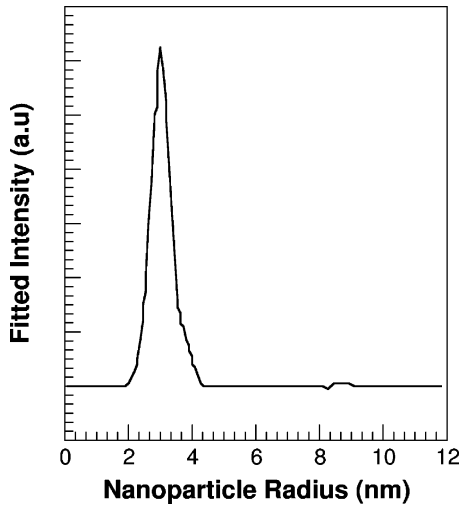

Figure 1. Particle size distribution of a hydrous zirconia nanoparticle solution ($\phi_{\text{nano}} = 1.85 \times 10^{-3}$) obtained from small-angle X-ray scattering data (ref 41).

Suspension Preparation. Aqueous binary suspensions are prepared by adding an appropriate volume fraction of nanoparticles to deionized water preadjusted with nitric acid (reagent grade, Fisher Scientific) to pH = 1.5. An appropriate volume fraction of a stock solution (pH = 1.5) of SiO_2 microspheres ($\phi_{\text{micro}} = 2.5 \times 10^{-3}$, 2.5×10^{-2}, 1.0×10^{-1}, and 2.5×10^{-1}) is then added followed by ultrasonication (model 550 sonic dismembrator, Fisher Scientific, Pittsburgh, PA). The suspensions are then stirred for 0.5 h followed by another ultrasonication step.

Binary suspensions are also prepared in an index-matched solution by first mixing an appropriate volume of deionized water (pH = 1.5) with a stock solution of glycerol that contained fluorescent dye (Rhodamine B, Sigma-Aldrich, St. Louis, MO). The ratio of water-to-glycerol is 1:2.8, as given by the Lorenz–Lorentz[44] index of refraction mixing rule. An appropriate volume fraction of nanoparticles is then added, followed by stirring for 10 min. Next, an appropriate volume fraction of colloidal microspheres is added, followed by ultrasonication. The suspensions are then stirred for 5 min followed by ultrasonication. Each sonication step consists of 2.5 min pulsed at a 1 s on/off sequence at 20 kHz.

Bulk Sedimentation. Colloidal silica microspheres ($\phi_{\text{micro}} = 1.0 \times 10^{-1}$) suspended in binary mixtures undergo gravity-driven sedimentation in glass cylinders (8 cm (H), 0.4 cm (D)) that are capped to minimize solvent evaporation. Initially, the samples are opaque (even those suspended in the index-matched solution)

(37) Hogg, R.; Healy, T. W.; Fuerstenau, D. W. Mutual Cuagulation of Colloid Dispersion. *Trans. Faraday Soc.* **1966**, *62*, 1683–1651.

(38) Sader, J. E.; Carnie, S. L.; Chan, D. Y. C. Accurate Analytic Formulas for the Double-Layer Interaction Between Spheres. *J. Colloid Interface Sci.* **1995**, *171*, 46–54.

(39) Hunter, R. J. *Foundations of Colloid Science*, 2nd ed.; Oxford University Press: New York, 2001.

(40) Peyre, V.; Spalla, O.; Belloni, L.; Nabavi, M. Stability of a Nanometric Zirconia Colloidal Dispersion under Compression: Effect of Surface Complexation by Acetylacetone. *J. Colloid Interface Sci.* **1997**, *187*, 184–200.

(41) Tohver, V. *Phase Behavior, Structure, and Properties of Colloidal Microsphere-Nanoparticle Mixtures*; University of Illinois: Urbana, IL, 2001.

(42) Miller, K. T.; Zukoski, C. F. Osmotic Consolidation of Suspensions and Gels. *J. Am. Ceram. Soc.* **1994**, *77*, 2473–2478.

(43) Gisler, T.; Schulz, S. F.; Borkovec, M.; Sticher, H.; Schurtenberger, P.; D'Aguanno, B.; Klein, R. Understanding colloidal charge renormalization from surface chemistry: Experiment and theory. *J. Chem. Phys.* **1994**, *101*, 9924–9936.

(44) Taslc, A. Z.; Djordjevic, B. D.; Grozdanlc, D. K. Use of Mixing Rules in Predicting Refractive Indices and Specific Refractivities for Some Binary Liquid Mixtures. *J. Chem. Eng. Data* **1992**, *37*, 310–313.

due to the scattering of visible light from the colloidal microspheres. As the samples settle, the suspension separates into a clear, microsphere-free supernatant, a cloudy solution, and an opaque sediment. This process is imaged using time-lapse photography with a video camcorder (Digital Handycam Camcorder, Sony, Japan) controlled by SupervisionCam software (Peter Kirst, Herrsching, Germany).

The initial microsphere settling velocity (V) is determined by tracking the interface separating the clear and cloudy solutions. Normalized values (V/V_{micro}) are reported to account for the large differences in solution viscosity between the aqueous and index-matched media and thereby facilitate direct comparison between these two systems. One can calculate V_{micro} using the Richardson−Zaki equation[45]

$$V_{micro} = V_0(1 - \phi_{micro})^n \quad (3)$$

where V_0 is the settling velocity for an isolated microsphere determined by Stokes' law

$$V_0 = \frac{2}{9}\frac{(\rho_s - \rho)a^2 g}{\eta} \quad (4)$$

ρ_s is the microsphere density, ρ is the density of the liquid phase, η is the apparent solution viscosity (η =1 mPa·s for water, 40 mPa·s for glycerol/water), g is the gravitational constant, and n is a power law exponent (=4.65). V_{micro} is found to be 5.8×10^{-4} and 1.1×10^{-5} mm/s for microsphere sedimentation from concentrated binary mixtures ($\phi_{micro} = 0.1$) in aqueous and index-matched solutions, respectively. Microsphere settling velocities (V_{micro}) are also determined from experimental observations for mixtures residing in the stable binary fluid phase, where settling of individual microspheres from suspension is observed. The minimum values of V_{micro} are found to be $\sim 3 \times 10^{-4}$ and 1×10^{-5} mm/s for aqueous and index-matched solutions, respectively. These experimental values, which are in good agreement with those predicted from eq 3, are utilized to determine the reported normalized settling velocity (V/V_{micro}). Finally, the sediment volume fraction ($\phi_{sediment}$) is determined by measuring the final sediment height at long times (>several weeks).

Colloidal Assembly. Colloidal silica microspheres suspended in binary mixtures are assembled under gravity-driven sedimentation in custom sample cells designed for confocal imaging. An appropriate volume of a given binary suspension is used as required to yield a final sedimentation height of nominally 150 μm for suspensions with $\phi_{micro} = 2.5 \times 10^{-3}$ and 2.5×10^{-2} and 1 mm for suspensions with $\phi_{micro} = 2.5 \times 10^{-1}$ (the sample volume required to create 150 μm sediments is too low at this ϕ_{micro}). Each cell is fabricated by attaching a glass tube (40 mm (H) × 8 mm i.d.) to a glass cover slip using poly(dimethylsiloxane) (PDMS) (Sylgard 184, Dow Corning, Midland, MI). Both the tubes and cover slips are cleaned prior to bonding by immersion in a 3:1 sulfuric acid (reagent grade, Fisher Scientific)/hydrogen peroxide (30% in water, Fisher Scientific) solution for 1 h. They are then rinsed repeatedly with deionized water, dried under a nitrogen stream, and bonded to one another using PDMS.

Imaging of Microsphere−Nanoparticle Mixtures. Confocal microscopy is used to image structures settled under gravity from binary mixtures of varying composition. The samples are analyzed both during assembly and after 3 weeks of sedimentation by placing them on the stage of an inverted optical microscope (Leica SP2 or DMIRB) equipped with 633 and 543 nm He/Ne laser sources and a 100×/1.4 NA oil lens. Images are acquired in reflection mode (633 nm excitation wavelength) for the aqueous samples and in fluorescent mode (543 nm excitation wavelength) for the index-matched samples. The samples are scanned in both the $x-y$ and $x-z$ directions, i.e., parallel and perpendicular to the glass substrate, respectively. Three-dimensional image stacks (total volume of 29 μm × 27 μm × 18 μm) are acquired in fluorescent mode with Δz of 0.1 μm between each 2-D slice. Five volumetric regions are scanned per sample with each volume containing between ~7000 and 10 000 particles depending on whether it resides in the gel or crystalline state.

Image Analysis. The confocal images are analyzed using IDL routines to filter the images and to locate particle positions in three dimensions.[46,47] The images are first filtered using a spatial band-pass filter to remove noise at high and low spatial frequencies. Each particle center is then located based on the regional intensity maxima. When the pixel intensity is averaged across the entire particle, its location can be identified with subpixel accuracy (~50 nm).[46]

3-D reconstructions (23 × 21 × 12.5 μm^3) are obtained for representative sediment structures. The sediment volume fraction is determined by dividing the total microsphere volume ($N_{tot} \times 4/3\pi a^3$, where N_{tot} is the total number of microspheres and $a = a_{micro}$) by the imaged volume and averaging this value over that obtained from five different scanned regions per sample. The pair correlation function $g(r)$ is determined by finding the number of microsphere centers inside a volumetric shell created a distance r away from a given microsphere center, relative to a uniform distribution of the same density. Each microsphere is checked against all other microspheres in a given scan volume over a total radius of 6 μm using dr = 0.01 μm as the shell thickness. Next, we identify nearest neighbors using the Delaunay triangulation method and calculate the Voronoi polyhedron volume associated with each particle.[28,48,49] By examining the orientation (bond angle and distance) between a given microsphere and its Delaunay nearest neighbors, one can also determine whether it resides in an amorphous or crystalline structure.[25] Adjacent particles with similar orientations of their neighbors are termed "ordered neighbors", and a particle with eight or more ordered neighbors is considered to be a crystalline particle.[25,50]

Results and Discussion

Microsphere−Nanoparticle Interactions. We first determine the effective interactions induced between microspheres in the presence of nanoparticle species in both aqueous and index-matched solutions in order to predict their respective phase behavior. Figures 2 and 3 show the effective microsphere potential V_{eff}/k_BT as determined from the colloidal pair correlation function obtained in the simulations. Colloidal many-body effects have been eliminated by performing these simulations in the dilute colloid limit. At low nanoparticle concentrations in water (Figure 2a), a repulsive barrier appears that increases with nanoparticle volume fraction. This is similar to what has been reported in ref 3 for a microsphere−nanoparticle size ratio of 100, although in the present case lower nanoparticle volume fractions are needed to achieve a comparable effective repulsion, due to the larger size ratio. Upon further increase of the nanoparticle concentration (Figure 2b), an attractive minimum appears in the potential, preceding the repulsive barrier. It was found in ref 3 that the depth of this minimum grows quadratically with ϕ_{nano}, indicating a *qualitative* difference with the linear concentration dependence exhibited by regular depletion interactions.[33,34] Examination of microsphere/nanoparticle configurations indicates that, upon approach of two microspheres, the halos remain largely unperturbed, and at a separation

(45) Guo, J. J.; Lewis, J. A. Aggregation Effects on the Compressive Flow Properties and Drying Behavior of Colloidal Silica Suspensions. *J. Am. Ceram. Soc.* **1999**, *82*, 2345−2357.

(46) Crocker, J. C.; Grier, D. G. Methods of Digital Video Microscopy for Colloidal Studies. *J. Colloid Interface Sci.* **1996**, *179*, 298−310.

(47) Dinsmore, A. D.; Weeks, E. R.; Prasad, V.; Levitt, A. C.; Weitz, D. A. Three-Dimensional Confocal Microscopy of Colloids. *Appl. Opt.* **2001**, *40*, 4152−4159.

(48) Preparata, F. P.; Shamos, M. I. *Computational Geometry*: *An Introduction*; Springer-Verlag: New York, 1985.

(49) Luchnikov, V. A.; Medvedev, N. N.; Naberukhin, Y. I.; Novikov, V. N. Inhomogeneity of the spatial distribution of vibrational modes in a computer model of amorphous argon, *Phys. Rev. B* **1995**, *51*, 15569−15572.

(50) Wolde, P. R. t.; Ruiz-Montero, M. J.; Frenkel, D. Numerical Calculation of the Rate of Crystal Nucleation in a Lennard-Jones System at Moderate Undercooling. *J. Chem. Phys.* **1996**, *104*, 9932−9947.

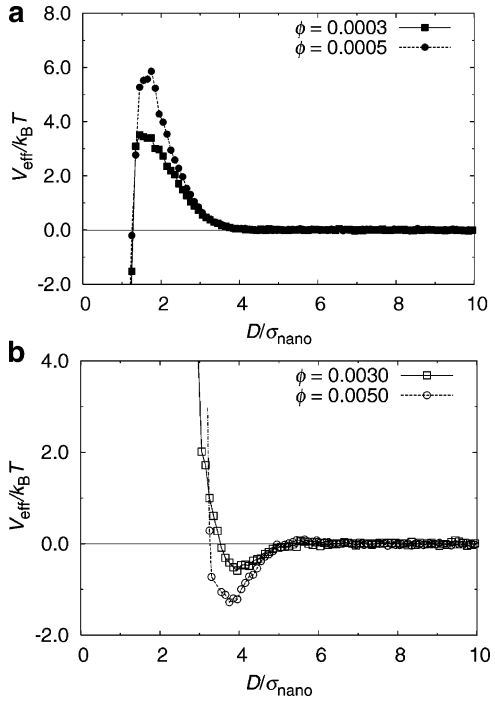

Figure 2. Effective potential V_{eff}/k_BT between microspheres suspended in aqueous solution in the presence of charged nanoparticles, as a function of the surface-to-surface separation D (in units of nanoparticle diameter σ_{nano}). (a) At low nanoparticle volume fraction ϕ, a repulsive barrier arises that increases with ϕ. (b) At higher nanoparticle volume fraction, an attractive minimum appears as well, with a strength that increases with increasing ϕ.

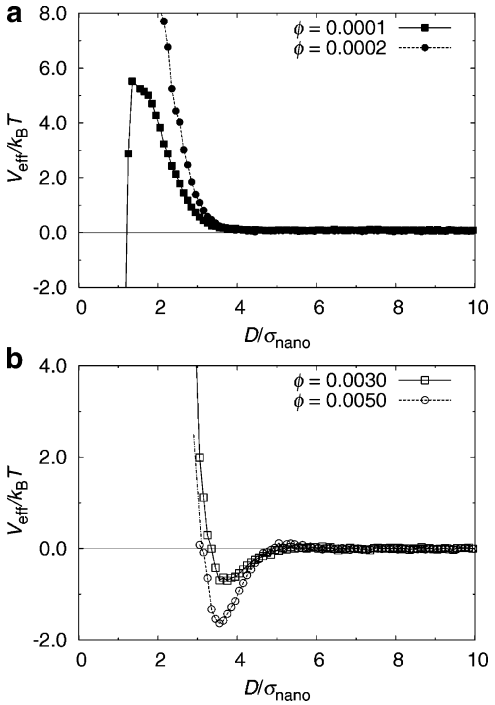

Figure 3. Effective potential V_{eff}/k_BT between microspheres suspended in an index-matched solution, as a function of the surface-to-surface separation D (in units of nanoparticle diameter σ_{nano}). (a) At low nanoparticle volume fraction ϕ, a repulsive barrier arises that increases with ϕ. (b) At higher nanoparticle volume fraction, an attractive minimum appears as well, with a strength that increases with increasing ϕ. Compared to an aqueous solution (Figure 2), both phenomena occur at lower volume fractions.

corresponding to the attractive minimum of the effective potential only limited nanoparticle depletion is observed in the region between the opposing halos.

In the index-matched solvent, V_{eff} varies in a similar way with nanoparticle volume fraction. For ϕ_{nano} as low as 10^{-4}, an effective barrier of approximately 5.5 k_BT is observed in the simulations (Figure 3a). Compared to the colloids suspended in water, lower nanoparticle concentrations are required to achieve a given induced repulsion. This is consistent with an enhancement in nanoparticle haloing around the microspheres, which in turn stems from the higher nanoparticle zeta potential employed in eq 2. The zeta potential is determined from the corresponding potential in aqueous solution under the assumption that the nanoparticle surface charge is independent of solvent composition. Because of our inability to assess the zeta potential in glycerol−water solutions, a more accurate value could not be obtained under these conditions. At higher ϕ_{nano} the attractive minimum is observed again (Figure 3b). While the concentration at which a certain potential minimum is achieved is also lower for the index-matched solution than under aqueous conditions, the difference between the two cases amounts to more than a simple shift of both phase boundaries. If we tentatively associate a barrier of 5 k_BT with the lowest nanoparticle volume fraction $\phi^{L,C}$ required to mitigate the intrinsic van der Waals attraction between the colloids, and a minimum of -2 k_BT with the nanoparticle volume fraction $\phi^{U,C}$ beyond which gelation occurs, we obtain a window of stability $\phi^{U,C}/\phi^{L,C} \approx 17$ in aqueous solution, whereas we find $\phi^{U,C}/\phi^{L,C} \approx 60$ for the index-matched solution. We note that the actual window for the latter is possibly even *larger*, as we have not taken into account the lowering of $\phi^{L,C}$ due to the weakening of the van der Waals attractions.

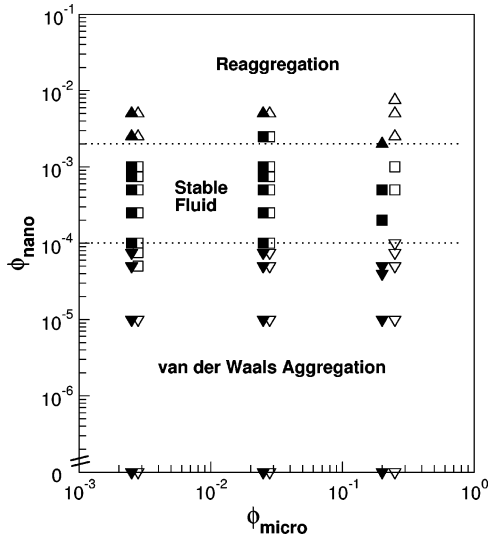

Figure 4. log−log plot of the phase behavior of microsphere−nanoparticle mixtures in both aqueous (filled symbols) and index-matched (open symbols) systems.

Phase Behavior of Microsphere−Nanoparticle Mixtures. The phase behavior of microsphere−nanoparticle mixtures of varying composition in aqueous and index-matched solutions is determined experimentally in order to make comparisons to the behavior predicted by simulations. The phase diagram, shown in Figure 4, is obtained by monitoring microsphere sedimentation in bulk samples and directly by using confocal microscopy. In the absence of nanoparticles, negligibly charged silica microspheres flocculate due to van der Waals interactions yielding clusters that settle rapidly to form a dense,

amorphous sediment. The van der Waals potential V_{vdW} for silica microsphere−microsphere interactions is calculated to be approximately $-60\ k_BT$ in aqueous and $-16\ k_BT$ in index-matched solutions, respectively, at a minimum separation distance of approximately 1 nm (cf. the approach outlined in ref 28). Below a lower critical nanoparticle volume fraction $\phi^{L,C}$, the system remains unstable, yielding a dense, amorphous sediment. This observation suggests that the microsphere interactions are indeed influenced by van der Waals forces, even in index-matched systems where they are substantially weakened. However, these forces decay very rapidly with increasing microsphere separation, and a nanoparticle-induced repulsive barrier, as demonstrated in Figures 2a and 3a, is sufficient to prevent aggregation. Indeed, at intermediate nanoparticle volume fractions ($\phi^{L,C} \leq \phi_{nano} < \phi^{U,C}$), the system resides in the stable fluid region from which individual colloidal microspheres settle under gravity to produce a crystalline sediment. The value of $\phi^{L,C}$ appears to be relatively insensitive to microsphere volume fraction or the solution in which they interact. Finally, above the upper critical volume fraction ($\phi_{nano} \geq \phi^{U,C}$), the system becomes unstable, once again yielding an amorphous structure upon sedimentation. This is consistent with the attractive minima observed in the simulations (Figures 2b and 3b) at higher nanoparticle concentrations. Upon quantitative comparison with the simulation results, we note a number of points. In view of the relatively coarse-grained model employed and the degree of arbitrariness involved (both in the simulations and experimentally) in locating the phase boundaries, the lower phase boundary $\phi^{L,C}$ for both solution compositions may be considered quite close to the concentrations in Figures 2a and 3a, although the simulations exhibit a solvent dependence for $\phi^{L,C}$ that is not observed in the experiments. The simulational results for the estimated upper phase boundary are rather similar for both cases and lie somewhat above the experimental estimate for $\phi^{U,C}$. As a result, the window of stability $\phi^{U,C}/\phi^{L,C}$ for the aqueous case has almost the same value in the simulations ($\approx$17) as in the experiments ($\approx$20), and the difference between simulation and experiment essentially amounts to a shift in nanoparticle concentration. In contrast, for the index-matched case there is a greater discrepancy between the $\phi^{U,C}/\phi^{L,C}$ value predicted by simulations ($\approx$60) and that observed experimentally ($\approx$20). This suggests that the extent of nanoparticle haloing, which the simulations find to be stronger in the index-matched solution, is actually rather similar in magnitude for both experimental systems. As mentioned above, this reflects our assumption regarding the nanoparticle charge in the index-matched case.

Interestingly, a broadening of the stable fluid region at lower microsphere volume fractions, as originally suggested by Tohver et al.,[30] is not observed. There is, however, a modest narrowing of this region at the highest microsphere volume fraction studied, in good accord with prior observations.[30]

Direct Imaging of Colloidal Assembly from Microsphere−Nanoparticle Mixtures. The structural evolution observed during gravity-driven assembly of colloidal microspheres from index-matched binary mixtures is monitored in situ using confocal microscopy over a broad concentration range. We report only the time evolution sequence for binary mixtures comprised of the lowest microsphere volume fraction studied ($\phi_{micro} = 2.5 \times 10^{-3}$), because of the fast dynamics at higher concentrations. The $x-y$ scans, shown in Figure 5, reveal the dramatic differences in structure observed for binary mixtures assembled from four different regions within the phase diagram, where $\phi_{nano} = 0$ (microspheres only), 10^{-5} (lower unstable region), 5×10^{-4} (stable fluid region), and 5×10^{-3} (upper unstable region). In these images, the colloidal microspheres appear as dark circular features against a surrounding lighter background that corresponds to the index-matched, fluorescent dye solution. In the absence of nanoparticle additions, the microspheres aggregate into stringlike clusters that are elongated in shape. This type of cluster formation leads to an initially open sediment structure, as shown in the $x-z$ scan depicted in Figure 6. However, this amorphous sediment ultimately densifies over time under its own weight, as microspheres continue to settle from solution. In sharp contrast, there is little evidence of cluster formation in binary mixtures that reside in the lower unstable region ($\phi_{nano} = 10^{-5}$). Despite being unable to visualize microsphere clusters in this sample, we observe that they exhibit a faster sedimentation rate than individual microspheres settling from the stable fluid phase ($\phi_{nano} = 5 \times 10^{-4}$). This is perhaps most obvious in the $x-y$ scans acquired at times of 120 and 180 min, in which there is a greater accumulation of colloidal microspheres at the substrate−sediment interface for the unstable mixture. A finite number of small clusters must form in mixtures that reside in the lower unstable region—otherwise there would be no difference in the rate of microsphere accumulation relative to the settling rate observed for individual microspheres in the stable region. This is confirmed by bulk sedimentation results (see Figure 8b) that reveal significantly higher settling velocities for microspheres in mixtures that reside in the lower (and upper) unstable regions than for those in the stable fluid phase. Finally, in the upper unstable region ($\phi_{nano} = 5 \times 10^{-3}$), there is again visual evidence in both the $x-y$ and $x-z$ scans that the microspheres form clusters, albeit far more compact in nature than those formed in the absence of nanoparticle additions. In this region, the microsphere clusters settle from suspension to form an amorphous sediment that is initially more open than that formed from either of the other mixtures, but significantly less open than that produced in the absence of added nanoparticles. Below, we comment on the origin of this difference. At the longest times probed (>3 weeks), only sediments assembled from the stable fluid phase are observed to crystallize. In all other cases, the final sediment consists of a dense, amorphous structure.

The microsphere−nanoparticle mixtures thus exhibit four distinct types of behavior during their assembly as the nanoparticle volume fraction increased: (1) aggregation leading to elongated clusters in the absence of nanoparticles, (2) aggregation leading to a large population of individual microspheres with some compact clusters at low nanoparticle concentrations, (3) a stable fluid phase at intermediate nanoparticle concentrations, and (4) aggregation leading to compact clusters at higher nanoparticle concentrations. These variations in cluster morphology stem from differences in the effective microsphere interactions as a function of ϕ_{nano}, following the sequence depicted in the simulational results (Figures 2 and 3). As microsphere interactions become more attractive, their sticking probability increases resulting in clusters that are more branched in nature. For the binary mixtures studied here, the strongest attractive interactions between microspheres occur in the absence of nanoparticle additions, where van der Waals forces dominate. Initial sediments assembled after a few hours of settling from dilute microsphere suspensions are most open, since there is ample opportunity for cluster growth prior to further consolidation as settling proceeds. In contrast, as the

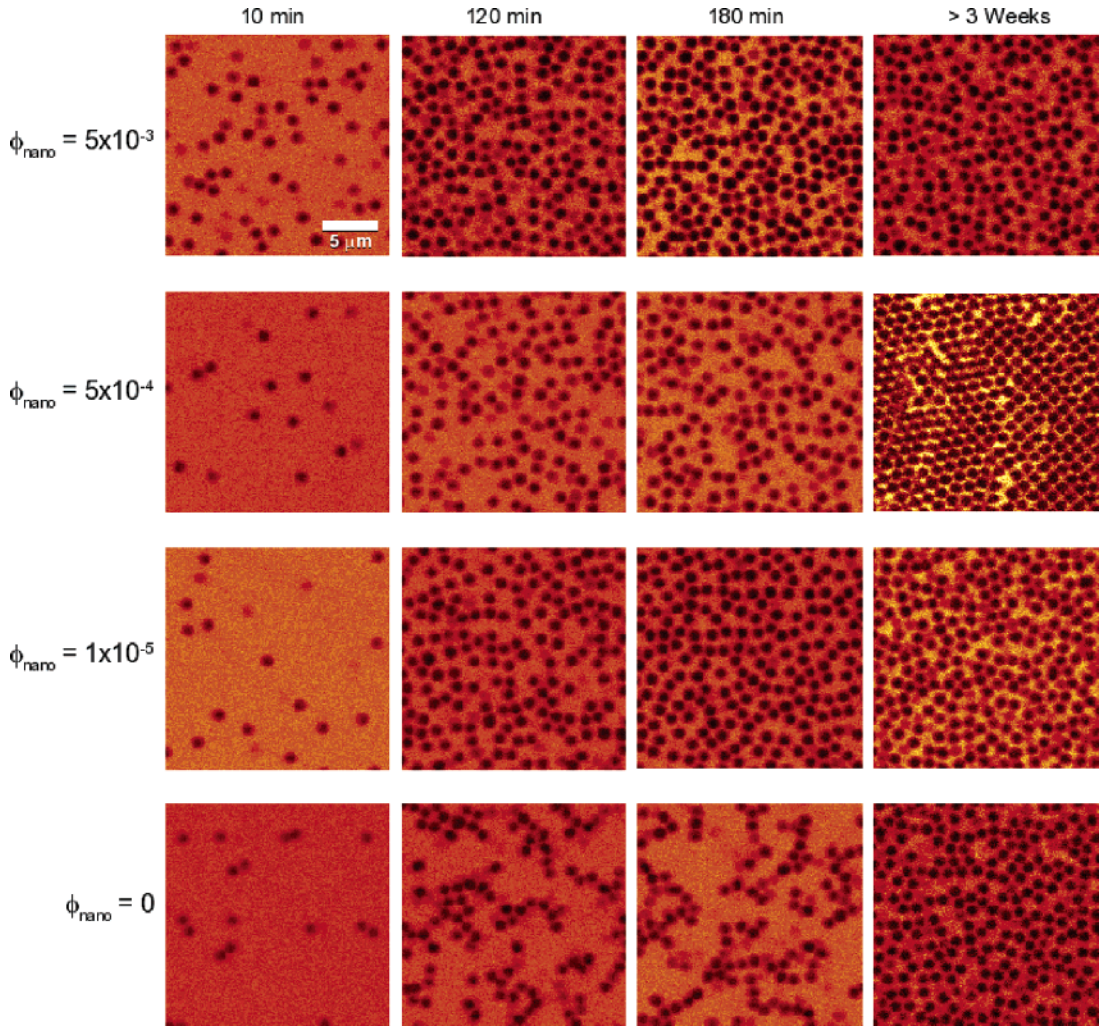

Figure 5. Confocal images of $x-y$ scans acquired at the sediment−substrate interface for structures assembled from binary mixtures comprised of $\phi_{micro} = 2.5 \times 10^{-3}$ and varying nanoparticle volume fraction (ϕ_{nano}) at different times during sedimentation.

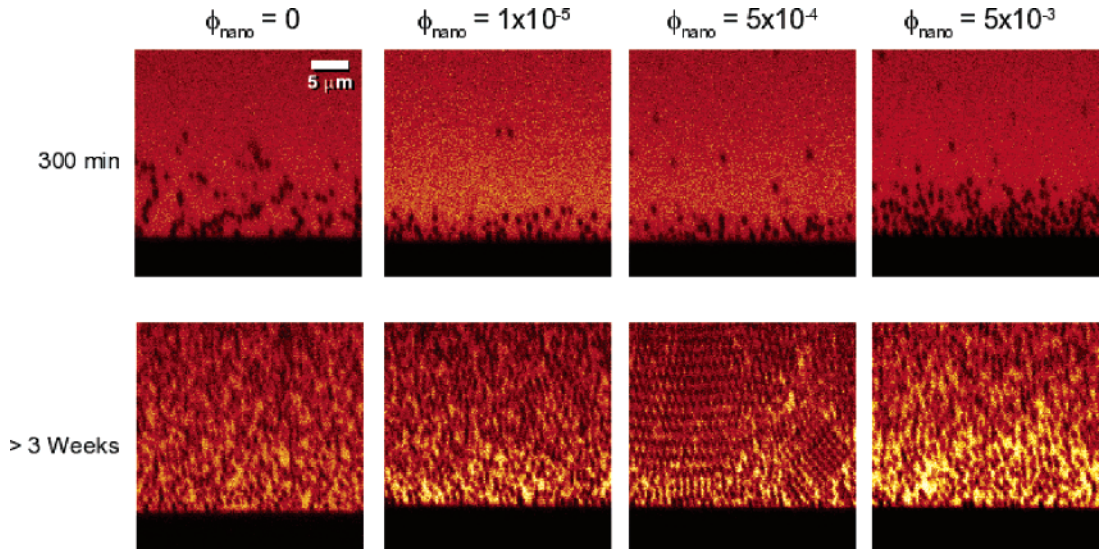

Figure 6. Confocal images of $x-z$ scans acquired through structures assembled from binary mixtures composed of $\phi_{micro} = 2.5 \times 10^{-3}$ and varying nanoparticle volume fraction (ϕ_{nano}) at different times during sedimentation.

microsphere concentration increases, cluster growth appears to be suppressed by enhanced sedimentation leading to initial sediment structures (~few hours) that are far more compact in nature (data not shown). As discussed below, the final structure of colloidal assemblies formed from these binary mixtures under gravity-driven sedimentation is influenced by their microsphere *and* nanoparticle concentrations. The dense structures observed at high nanoparticle concentrations are compatible with the interaction profiles in Figures 2b and 3b, where it was observed that, in addition to the shallow attractive minimum (which is presumably responsible for the

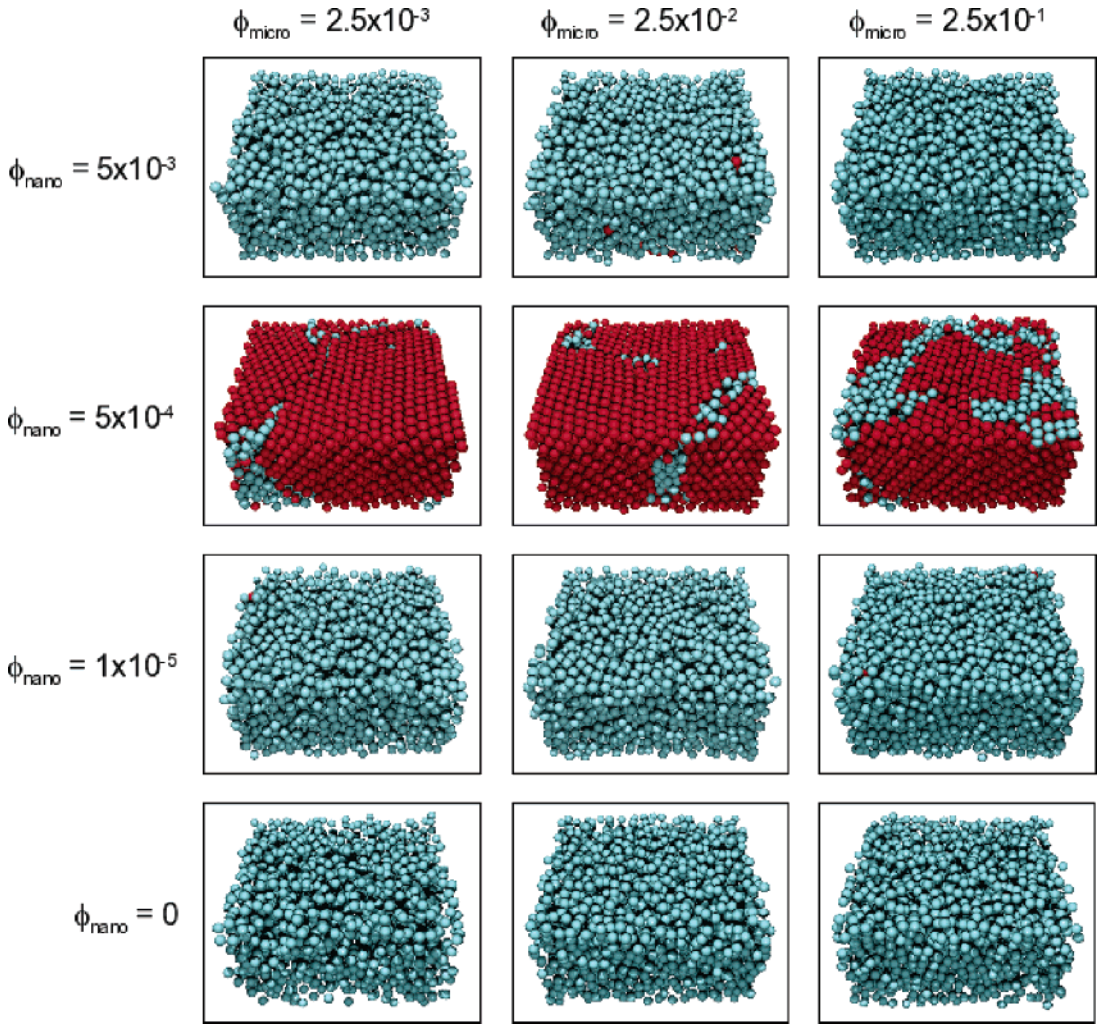

Figure 7. 3-D reconstructions of sediment structures assembled from binary mixtures composed of varying microsphere (ϕ_{micro}) and nanoparticle (ϕ_{nano}) volume fractions.

aggregation behavior), a strong *repulsive* barrier is still present, suggesting that the (considerably stronger) van der Waals interactions continue to be (partially) mitigated in the upper part of the phase diagram.

Structure of Colloidal Phases Assembled from Microsphere–Nanoparticle Mixtures. We systematically analyze the final sediment structures assembled from binary mixtures to quantify the effects of microsphere and nanoparticle concentration within each region of the phase diagram reported in Figure 4. 3-D reconstructions for representative sections of sediments assembled from these mixtures are shown in Figure 7. They are color-coded to distinguish colloidal particles in disordered (blue) and crystalline regions (red). Crystalline structures are observed only for samples that settle from binary mixtures that reside in the stable fluid region. The 3-D reconstructions reveal the polycrystalline nature of sediments formed from within this region, with blue particles highlighting domain boundaries that exist at the interface between single crystal domains. Outside this region, the sediments are comprised of dense, amorphous structures (or gels). Because it is difficult to discern the subtle effects of varying composition on the 3-D structure of either the crystalline or amorphous sediments solely from these images, we further analyze the imaged volumes to determine their sediment volume fraction, radial distribution function, Voronoi polyhedra volume, and local bonding structure.

The sediment volume fraction, $\phi_{sediment}$, is plotted in Figure 8a for samples assembled from binary mixtures of varying composition. For comparison, data acquired directly from confocal images of samples formed from binary mixtures suspended in the index-matched medium is shown along side data determined by bulk sedimentation of binary mixtures in both aqueous and index-matched solutions. Not surprisingly, the most open sediment structure (~30 vol %) forms for pure microspheres settling in an aqueous solution. When the microspheres settle in an index-matched solution, open sediments of density (~35 vol %) similar to those reported for the aqueous system are observed only for the most dilute sample studied. Enhanced consolidation occurs with increasing microsphere volume fraction leading to sediment densities of ~35%, 43%, and 51 vol % for sediments produced from initial microsphere suspensions of 2.5×10^{-3}, 2.5×10^{-2}, and 2.5×10^{-1}, respectively. With increasing nanoparticle volume fraction, the sediment density increases until a plateau value of roughly 60 ± 3 vol % is reached for mixtures of all compositions settling within the stable fluid phase. In contrast, the maximum densities (~53–57 vol %) observed for sediments formed during bulk sedimentation (initial $\phi_{micro} = 10^{-1}$) from both aqueous and index-matched systems are considerably lower in this region. In the upper unstable region, the sediments become increasingly more open with further increases in nanoparticle volume fraction. At a given nanoparticle concentration, denser sediments are observed for mixtures with higher initial microsphere volume fraction in both the lower and upper unstable regions of the phase diagram.

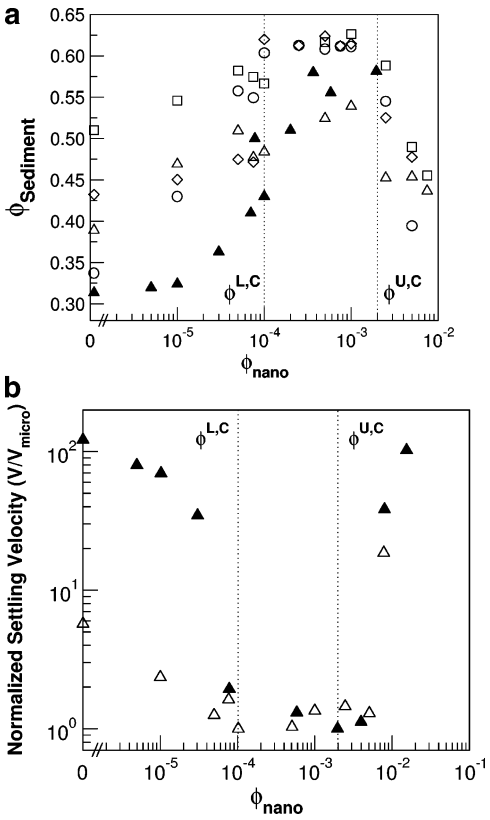

Figure 8. (a) Sediment volume fraction ($\phi_{sediment}$) as a function of nanoparticle volume fraction (ϕ_{nano}) for structures assembled from binary mixtures (○) $\phi_{micro} = 2.5 \times 10^{-3}$, (◇) $\phi_{micro} = 2.5 \times 10^{-2}$, (△) $\phi_{micro} = 1 \times 10^{-1}$, and (□) $\phi_{micro} = 2.5 \times 10^{-1}$ suspended in an index-matched solution and binary mixtures (▲) $\phi_{micro} = 1 \times 10^{-1}$ suspended in an aqueous solution, where triangular data points correspond to bulk sedimentation results. (b) Normalized settling velocity (V/V_{micro}) as a function of nanoparticle volume fraction (ϕ_{nano}) during initial sedimentation of binary mixtures ($\phi_{micro} = 1 \times 10^{-1}$) suspended in aqueous (▲) and index-matched solutions (△).

Interestingly, the sediment densities in the absence of nanoparticles and at the highest nanoparticle volume fraction ($\sim 10^{-2}$) investigated are quite comparable for the index-matched systems, suggesting that the strength of the attraction in both limits is similar (of the order of several k_BT), despite the fundamentally different origin of the interaction.

The initial microsphere settling velocities depend strongly on both nanoparticle volume fraction and solution composition, as shown in Figure 8b. As stated previously, these data are presented in a normalized fashion to facilitate direct comparison between aqueous and index-matched binary mixtures. In the absence of nanoparticle additions, the normalized settling velocity is approximately 100- and 6-fold higher than for individual microsphere sedimentation from the stable fluid phase in aqueous and index-matched systems, respectively. These values reflect the formation of particle clusters in suspension driven by van der Waals attractions between microspheres. Because the microsphere volume fraction is identical in both systems, the higher settling rates observed for aqueous suspensions are attributed to enhanced cluster formation compared to the index-matched suspensions. This is not unexpected given the suppression of the van der Waals attractions in the latter system. In the lower unstable region, the normalized settling velocity decreases as a function of increasing nanoparticle volume fraction until a value of unity is approached at the critical lower nanoparticle volume fraction $\phi^{L,C}$. This decrease in velocity is directly linked to diminished cluster formation, resulting from the effective potential barrier (Figures 2a and 3a) that in turn arises from nanoparticle halo formation. Within the stable fluid phase, both systems exhibit normalized settling velocities of roughly unity, corresponding to the sedimentation of individual microspheres in these samples. Finally, at higher nanoparticle volume fractions ($\phi_{nano} > \phi^{U,C}$), the normalized settling velocity increases with increasing nanoparticle volume fraction, as the effective microsphere attraction intensifies, leading to enhanced cluster formation. The rapid nature of this increase can be understood from the simulation results (cf. Figures 2b and 3b and ref 3), which indicate that the microsphere attraction increases superlinearly with nanoparticle concentration.

The microsphere pair correlation functions $g(r)$ of sediments assembled from binary mixtures of varying composition are reported in Figure 9. The peaks in $g(r)$ indicate ordering of particles into coordination shells. The data for crystalline sediments assembled from binary mixtures that reside in the stable fluid phase possess features characteristic of a well-ordered structure; i.e., the particles are organized in multiple coordination shells around a given central particle. As the microsphere volume fraction increases, the degree of order observed for these crystalline sediments lessens slightly, as indicated by a modest broadening of the first and higher order peaks. In contrast, the $g(r)$ shown for sediments assembled from binary mixtures that reside in the lower or upper unstable regions of the phase diagram possess features characteristic of a dense liquid structure. There are subtle differences between these data. For example, the first peak in $g(r)$ is broadest in the amorphous sediment structures formed in the absence of nanoparticles or at the highest nanoparticle volume fraction probed for systems with the lowest microsphere volume fraction. However, more striking is the similarity in $g(r)$ for sediments assembled within both the lower and upper unstable regions near their respective phase boundaries. Important differences do emerge, however, when analyzing the heterogeneity of these weak gels via Voronoi tessellation.

van Blaaderen and Wiltzius[20] and Varadan and Solomon[22] were first to apply Voronoi tessellation to spatially characterize the respective structures of colloidal glasses and dense colloidal gels. The peak value in the Voronoi polyhedral (VP) volume distribution reflects the average VP volume available to colloidal microspheres within these dense sediment structures, whereas the standard deviation and skewness of the distribution are indicative of their structural inhomogeneity, as shown in Figure 10. The VP volume distributions for amorphous sediments formed from binary mixtures in the lower or upper unstable regions exhibit a distribution that is broader than that observed for crystalline sediments formed from binary mixtures that reside in the stable fluid phase. Correspondingly, their values are also higher, indicative of greater structural heterogeneity. It is illustrative to first examine these data for sediments formed from pure microsphere suspensions of varying ϕ_{micro}. The VP volume distribution is broadest for sediments produced from the most dilute microsphere suspension and narrows significantly with increasing ϕ_{micro}. Correspondingly, the σ values reported for the pure microsphere sediments systematically decrease from 0.7 to 0.29 μm^3 with increasing ϕ_{micro}, which reflects the enhanced structural homogeneity of gels at higher density (or $\phi_{sediment}$). As the nanoparticle volume fraction is increased in the lower unstable region, the sediment structures densify to yield more homoge-

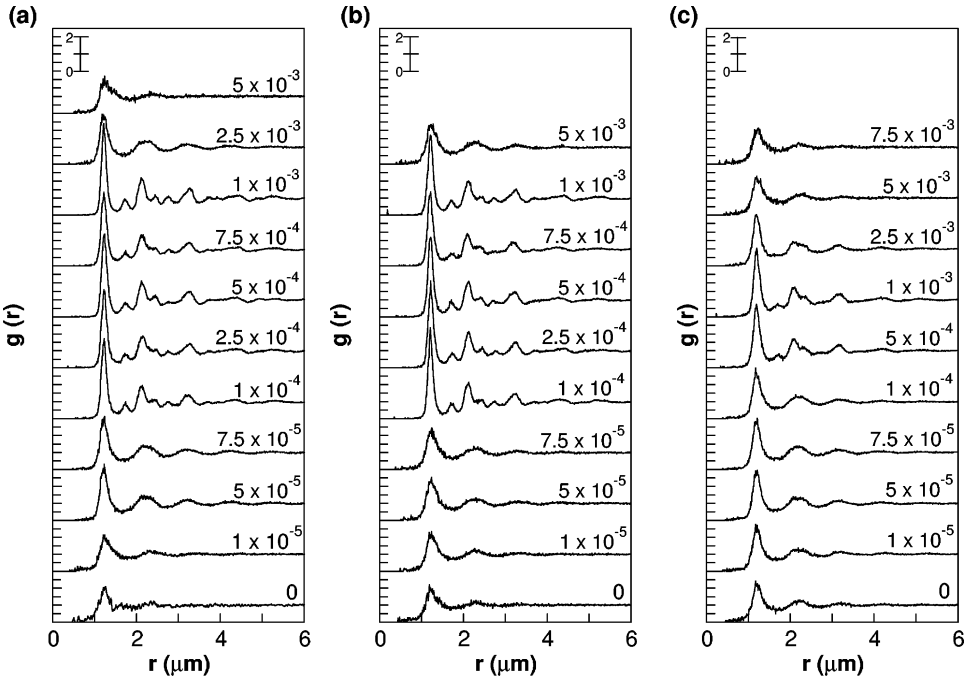

Figure 9. Radial distributions acquired on structures assembled from binary mixtures with (a) $\phi_{micro} = 2.5 \times 10^{-3}$, (b) $\phi_{micro} = 2.5 \times 10^{-2}$, and (c) $\phi_{micro} = 2.5 \times 10^{-1}$ with varying nanoparticle volume fraction (ϕ_{nano}, as specified).

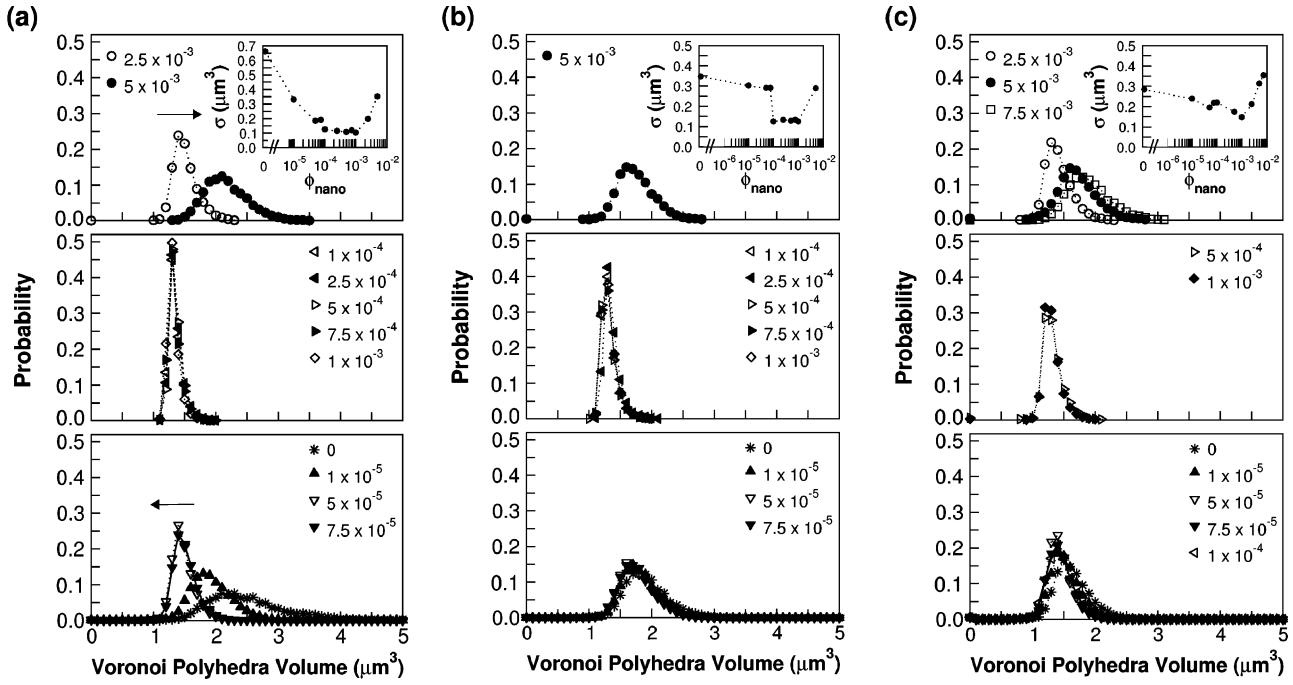

Figure 10. Probability distribution of Voronoi polyhedra volume for structures assembled from binary mixtures comprised of (a) $\phi_{micro} = 2.5 \times 10^{-3}$, (b) $\phi_{micro} = 2.5 \times 10^{-2}$, and (c) $\phi_{micro} = 2.5 \times 10^{-1}$ with varying nanoparticle volume fraction (ϕ_{nano}, as specified). The insets show the standard deviation of the experimental data as a function of ϕ_{nano}. Arrows denote direction of increasing nanoparticle volume fraction.

neous structures, as reflected by a shift in their VP peak to lower values and a simultaneous reduction in their σ values. The VP volume distributions for crystalline sediments assembled from binary mixtures that reside in the stable fluid region possess features characteristic of a well-ordered structure, i.e., a very narrow distribution with a peak at $\sim$1.2 μm^3 and values of $\sim$0.1 μm^3. This is close to the minimum value of 1.16 μm^3 expected for microsphere crystals that adopt an face-centered cubic (or hexagonal close packed) packing geometry. As the microsphere volume fraction increases, these crystalline sediments become less ordered, as indicated by a decrease in VP peak intensity. Finally, in the upper unstable region, there is a systematic shift to a broader VP volume distribution and higher values with increasing nanoparticle volume fraction. In this region, the observed changes appear to be less sensitive to microsphere volume fraction.

The number of nearest-neighbor (#NN) bonds per particle is depicted in Figure 11 for sediments assembled from binary mixtures of varying composition. This quantity provides insight into the degree of structural rearrangement at the local scale.[27] The local topology of colloidal gels should be dominated by chainlike aggregates

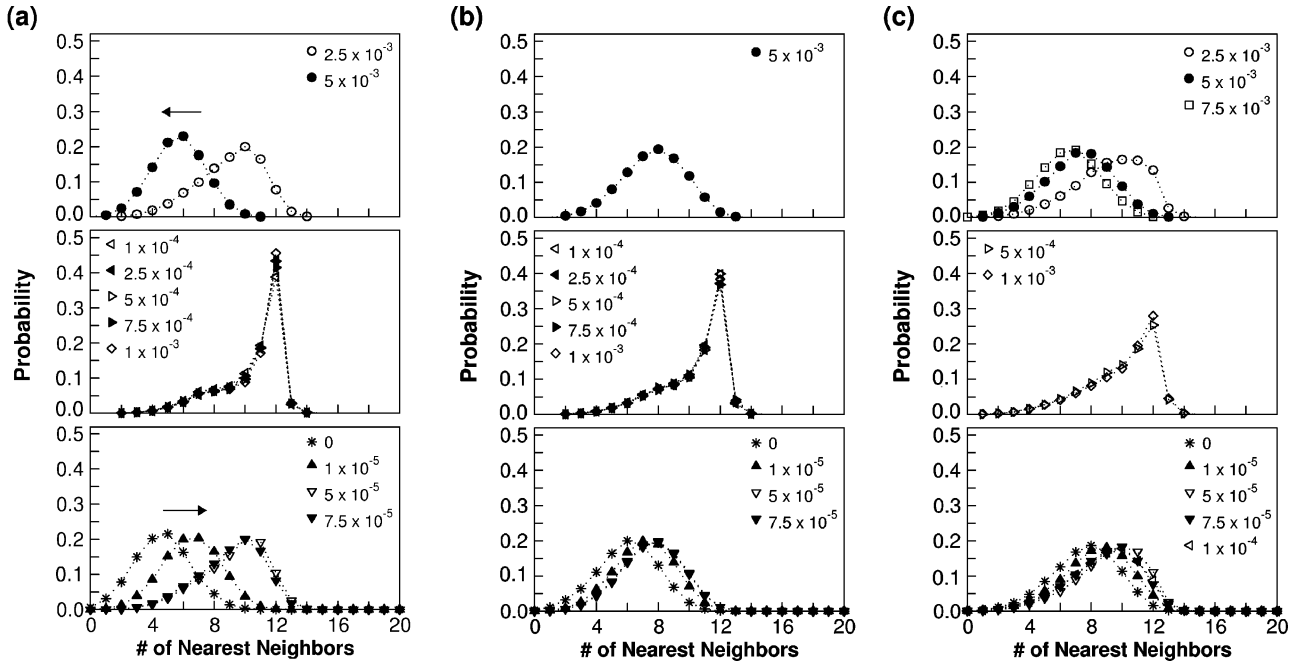

Figure 11. Probability distribution of the number of nearest neighbors for structures assembled from binary mixtures comprised of (a) $\phi_{micro} = 2.5 \times 10^{-3}$, (b) $\phi_{micro} = 2.5 \times 10^{-2}$, and (c) $\phi_{micro} = 2.5 \times 10^{-1}$ with varying nanoparticle volume fraction (ϕ_{nano}, as specified). Arrows denote direction of increasing nanoparticle volume fraction.

(#NN = 2) if the particle−particle bonds are rigid and irreversible. In sharp contrast, if particles within a given cluster can rearrange by, for example, rotation, then significant compaction and reorganization can occur. In the absence of nanoparticles, a chainlike morphology is observed during the initial stage of sedimentation of dilute microsphere suspensions ($\phi_{micro} = 2.5 \times 10^{-3}$); see Figure 5. However, at longer sedimentation times (>3 weeks), these sediment structures experience substantial consolidation yielding a final #NN bonds of ~4 and a $\phi_{sediment}$ of ~0.35. In the lower unstable region, the peak in the #NN distribution increases with increasing nanoparticle volume fraction within these dense amorphous sediments. This observation suggests an overall weakening of microsphere−microsphere bonds with increasing ϕ_{nano} in this region of the phase diagram. In the stable fluid region, the peak in the #NN distribution occurs at a value of 12, which is expected given their crystalline nature. There is no discernible dependence on nanoparticle volume fraction in this region, but there is a modest broadening of the #NN distribution with increasing microsphere volume fraction. This trend likely reflects the fact that the microspheres become increasingly trapped in nonequilibrium positions during sedimentation under these conditions. Finally, in the upper unstable phase region, the opposite trend emerges with the #NN distribution shifting toward lower peak values with ϕ_{nano}. Suppressed bond rotation is expected due to intensified microsphere−microsphere attractions deeper within the upper phase region. Our observations are in good agreement with those reported by Weitz and co-workers[27] for depletion gels formed from colloidal−polymer mixtures.

Conclusions

We have investigated the interparticle interactions, phase behavior, and structure of binary microsphere−nanoparticle mixtures that possess both high charge and size asymmetry. Through compositional tailoring, we have created both colloidal gels and crystals by gravity-driven sedimentation of colloidal microspheres in aqueous and index-matched solutions on flat substrates. The use of an index-matched, fluorescent dye solution is required to facilitate 3-D imaging and structural analysis of the as-assembled colloidal phases. However, a direct consequence of index matching is that the strength of the van der Waals attraction between microspheres is lessened considerably relative to their interaction in aqueous solution. Thus, the colloidal gels that form in the absence of nanoparticle additions (or at low concentrations) are relatively weak yielding amorphous structures that densify considerably under their own weight. At intermediate nanoparticle concentrations, the colloidal microspheres are fully stabilized and form a polycrystalline array upon sedimentation. Within this region (which spans over a decade in nanoparticle volume fraction), there is surprisingly little effect of nanoparticle concentration on the observed 3-D crystal structure or sediment density. In sharp contrast, the degree of crystallinity declines with increasing microsphere volume fraction, as evidenced by a substantial broadening of the distributions of both the Voronoi polyhedra volumes and number of nearest neighbors. These observations have important implications for our parallel efforts, which exploit the nanoparticle-mediated assembly of colloidal microspheres on epitaxially patterned substrates.[31] Namely, the structural evolution of colloidal crystals assembled from stable (fluid) mixtures depends far more critically on microsphere concentration than on nanoparticle concentration. In the lower and upper unstable regions, the driving force for microsphere flocculation stems from van der Waals interactions and effective, nanoparticle-induced interactions, respectively, as we have demonstrated by direct simulation of microspheres in the presence of various nanoparticle concentrations. The nanoparticles initially only induce a repulsive barrier that increases in strength with increasing nanoparticle concentration, but at higher concentrations an effective attraction appears as well. Therefore, the structural evolution of colloidal gels assembled from binary mixtures in these two regions exhibits the opposite dependence on nanoparticle concentration, such that denser gels form with increasing nanoparticle volume fraction in the lower unstable region whereas more open

gels form with increasing nanoparticle volume fraction in the upper unstable region. The ability to tune the phase behavior and structure of colloidal phases through nanoparticle engineering broadens the palette of systems that can be used as precursors for assembling ceramic, photonic band-gap, and pharmaceutical materials, as well as novel inks and coatings.

Acknowledgment. This material is based upon work supported by the U.S. Department of Energy, Division of Materials Science under Award Nos. DEFG02-91ER45439 through the Frederick Seitz Materials Research Laboratory at the University of Illinois at Urbana-Champaign and by NSF (Grant 00-71645). S. K. Rhodes is supported by an NSF Graduate Fellowship and J. Liu by NSF-CAREER Award No. DMR-0346914 to E. Luijten. E. R. Weeks is supported by NSF-CAREER Award No. DMR-0239109. E. Luijten acknowledges computing time on the NSF TeraGrid facility at the National Center for Supercomputing Applications under Award No. TG-DMR040030T. J. A. Lewis acknowledges the experimental assistance of V. Tohver and P. Jemian (Argonne National Laboratory), who carried out USAXS measurements and particle size analysis on the nanoparticle species in solution and James Gilchrist, who assisted with confocal measurements.

LA050382S